Thermoplastic deformation and structural evolutions in nanoimprinting metallic glasses using molecular dynamics analysis

CrossMark

Yiying Zhu [a], Guanglan Liao [a], Tielin Shi [a], Mo Li [b], Zirong Tang [a], Feng Xiong [a],*

[a] State Key Laboratory of Digital Manufacturing Equipment and Technology, Huazhong University of Science and Technology, Wuhan 430074, China
[b] School of Materials Science and Engineering, Georgia Institute of Technology, Atlanta, GA 30332-0245, USA

ARTICLE INFO

ABSTRACT

We perform simulations on nanoimprinting metallic glasses to investigate the thermoplastic deformation and structural evolutions via molecular dynamics analysis. The atomic diffusion mechanisms, including single atomic and highly collective hopping, are observed in metallic glass block. Mold filling speed is significantly affected by the initial metallic glass film thickness, and the film with the thickness approaching the width of the pattern on mold is optimal to shorten mold filling time and save materials. With the support of a modified equation of plane Poiseuille flow, we analyze the resistance of boundary condition and capillary force, which have reasonably explained the thickness effect. We then show the structural evolutions to assess the impact of the mold filling process on the short-range and the middle-range orders in metallic glasses. Lower fractions of icosahedra and icosahedra-like clusters and smaller aggregated clusters have been detected in the processed structure than in the billets, showing that the processed metallic glasses are more symmetrical and have more disorder. The results further suggest that the mold filling process has broken the original structures in metallic glasses, resulting in less icosahedra and bond networks, which lead to a better plasticity in the processed metallic glasses.

© 2015 Elsevier B.V. All rights reserved.

1. Introduction

Nanoimprint possesses many advantages such as high resolution and low cost over other traditional methods in fabricating micro-/nano-structures, and has been a promising way to achieve micro-/nano-structure integration systems [1]. The polymer is the original material in nanoimprint [2,3], in which the ultimate feature size is fundamentally limited by the length of the resist molecule [4]. Metallic glasses (MGs), which have no size limiting factor, are superplastic in the super-cooled liquid region, showing the ability to replicate smaller features including nanoscale structures such as nano-grating [5]. With high strength, good surface quality, excellent wear and corrosion resistance in nanoscale compared with polymer, MGs can be used in nanoimprint and greatly improve the quality of micro-/nano-structures [6].

Till now, the effects of pressure, viscosity, temperature and dimensions of stamp on nanoimprint have been well analyzed through experiments [7], finite element analysis [8] and molecular dynamic (MD) analysis [9,10]. The imprint objects are mainly alloy or polymer and the influence of capillary force is rarely noted. Some works have been carried out to fabricate MG structures via nanoimprint, and good micro-/nano-sized structures are obtained [11–14]. The MGs show enormous potential in micro-molding. J. Schroers et al. reported

13 nm MG structures fabricated by nanoimprint and firstly combined the capillary contribution to Hagen-Poiseuille's law to describe nanoimprinting MGs [5]. Subsequently, they built a quantitative model for the thermoplastic compression molding process using lubrication theory [15]. Although the mold filling process is well studied, present understanding of atomic migration, which can reflect the influences of capillary contribution and may be helpful to optimize the nanoimprint parameters, is rather incomplete. Furthermore, MGs have low plasticity at room temperature, leading to obvious brittleness which is regarded as an intrinsic defect of MGs and severely limits their application [16]. Evidences are obtained that the inner atomic order can reflect the performance of MGs. The icosahedra (ICO) are considered to be the dominated short-range order in MGs [17]. It is reported that the ICO are resistant to the atomic migration and the MGs with low fraction of ICO readily accept the shear transformation [18,19]. The ICO clusters tend to overlap together forming the medium-range order in MGs and the network of aggregated clusters is also a significant influence factor on the mechanical property [20,21]. Thus, the research about structural evolutions in MGs during the mold filling process becomes very meaningful.

In this article, we construct a numerical nanoimprint model to investigate the atomic migration of MGs. The effect of the thickness of initial billet film (TF) on nanoimprinting MGs is discussed and a rule is proposed for selecting the thicknesses to perform an efficient and economical filling process. The boundary condition and the capillary contribution are observed playing important roles in the process. We

* Corresponding author.
  E-mail address: xfzlmm@hust.edu.cn (F. Xiong).

Table 1
Parameters of LJ potential of Zr, Cu and Si.

Species	ε (eV)	σ (Å)
Zr	0.7382	2.9318
Cu	0.409	2.338
Si	0.0175	3.826
Si–Zr	0.1137	3.3789
Si–Cu	0.0846	3.082

also study the structural evolutions of MGs in the filling process, including the short-range order and middle-range order, to assess the change of performance of MGs during the thermoplastic deformation.

2. MD simulations

The model consisted of three types of atoms, Cu, Zr and Si, where three potential functions were used. The embedded atom model (EAM) potential was adopted to describe the interactions between Zr–Zr, Zr–Cu, and Cu–Cu, which was developed by Mendelev et al. and widely used [22,23]. The stamp composing of silicon atoms was introduced, where the interaction between Si–Si was determined by Tersoff potential [24]. The interaction between Si–Cu was evaluated by the Lennard-Jones (LJ) potential, and so did Si–Zr. The parameters of Zr, Cu and Si for LJ potential were listed in Table 1, where the pair parameters were obtained using the Lorenz–Berthelot mixing rule [25].

A configuration with the size of $67 \times 67 \times 67$ Å^3 consisting of 16,000 atoms was built to prepare MGs through a rapid cooling process, in which the atom ratio of Cu:Zr was 46:54. Periodic boundary condition was applied in three dimensions and the Nose–Hoover algorithm was used to control temperature and pressure. The time step was set as 1 fs. The Cu$_{46}$Zr$_{54}$ block was melted (at 2100 K) at first and then quenched to 300 K at a cooling rate of 2 K/ps under pressure of 0 Pa. The partial pair distribution functions of the Cu$_{46}$Zr$_{54}$ are plotted in Fig. 1a. The splitting of second peaks is observed in the Cu–Cu, Zr–Zr and Cu–Zr curves. The first-neighbor bonds calculated from the positions of first peaks are $r_{Cu–Cu} = 2.57$ Å, $r_{Zr–Zr} = 3.17$ Å and $r_{Cu–Zr} = 2.81$ Å, consistent with the experimental and emulational values [23,26], indicating that the potential is appropriate for describing the Cu–Zr MGs. The elastic coefficients are calculated using fluctuation formula [27] after equilibration of 10 ps. The shear modulus at temperature of 300 K is about 30 GPa, in good agreement with the results in reference [28]. The average atomic volume changes with temperature during the cooling process, as shown in Fig. 1b. The intersection point of the fitting lines locates the glass transition temperature T_g, about 839 K, higher than the experimental result of 696 K due to much higher cooling rate [29]. The inset in Fig. 1b shows the temperature dependence of the self diffusion coefficients for Cu and Zr. With a smaller atomic radius and mass, Cu always obtains a larger diffusion coefficient than Zr. The break of the lines corresponds to the glass transition region. Under this break the block turns to a solid amorphous alloy.
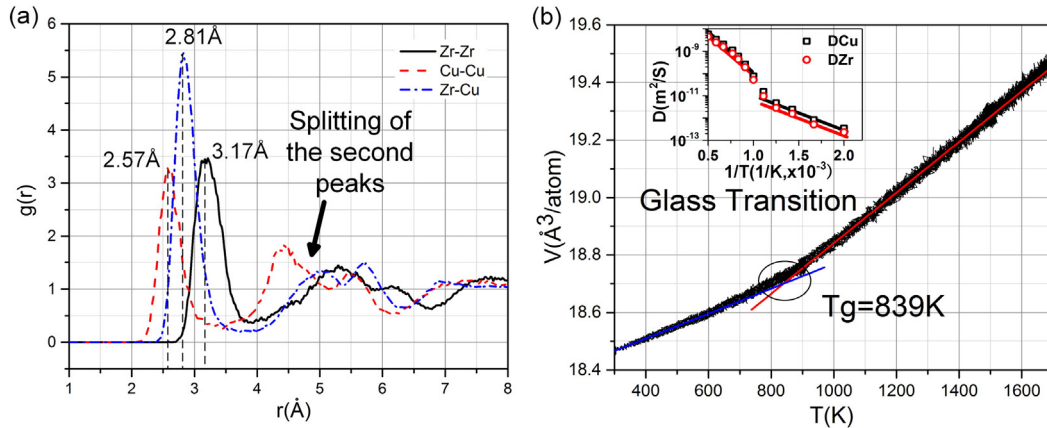
Fig. 1. (a) The partial pair distribution functions of the Cu$_{46}$Zr$_{54}$ block at 300 K and (b) the average atomic volume of the Cu$_{46}$Zr$_{54}$ block during the cooling process.
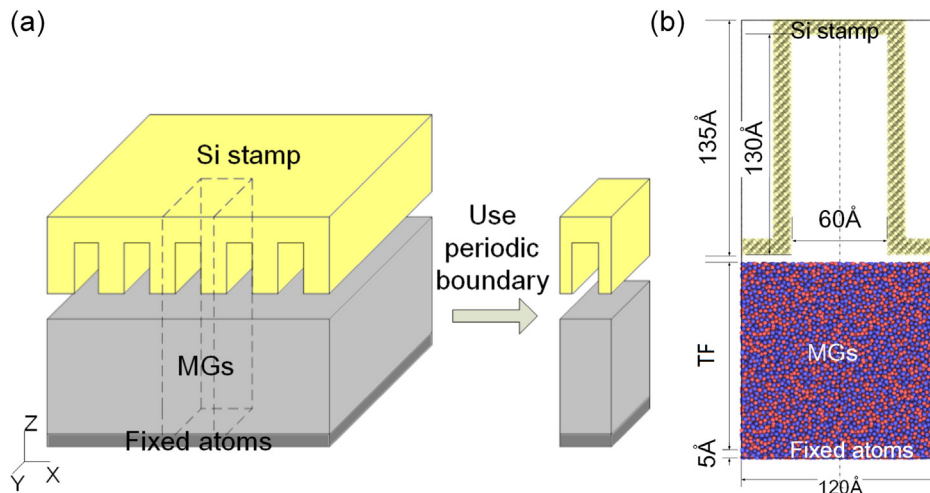
Fig. 2. The nanoimprint simulation model: (a) schematics diagram for simplification and (b) the atomic view with detailed dimensions.

The nanoimprint simulation model was then constructed, which consisted of a silicon stamp and a film of $Cu_{46}Zr_{54}$ MGs obtained from the amorphous block, as shown in Fig. 2a. The pattern on the stamp was a groove array, thus the nanoimprint process of a single groove could be regarded as a closed extrusion. The periodic boundary condition was prescribed to four sides at X and Y directions with the width of 120 Å and 25 Å to improve calculation efficiency. The time step was also set as 1 fs and the temperature was kept about 800 K just around T_g. The stamp was defined as rigid body, in which the silicon atoms not contacting the MGs were removed for simplification. All detailed dimensions are marked clearly in Fig. 2b, where the width of the groove (Wg) is 60 Å and the height of the groove is 130 Å.

The simulations were performed in force-controlled mode. The stamp was held at the maximum height for 10 ps at first. Force was then exerted on the stamp for 250 ps. The TF was set in a range from 45 Å to 300 Å and the force was set as 32 nN, 48 nN and 64 nN,

respectively. 32 nN force brought about 1 GPa pressure on the stamp, much higher than that in the actual imprint process (about 50 MPa). The extremely high pressure was a compelled choice under inherent limitation of MD in time-scale. The grating height (H) data were obtained by calculating the difference between the Z coordinates of the atoms on the top and foot of the grating. Pressure, density and structure information were recorded during the simulation. Here the parallel MD code LAMMPS [30] was used throughout the study.

3. Results and discussion

3.1. Thermoplastic deformation

Fig. 3 shows the snapshots of the nanoimprint process cutaway views during the simulation with $TF = 120$ Å under 48 nN force. In Fig. 3a, the Van der Waals force drives the MG atoms to contact with
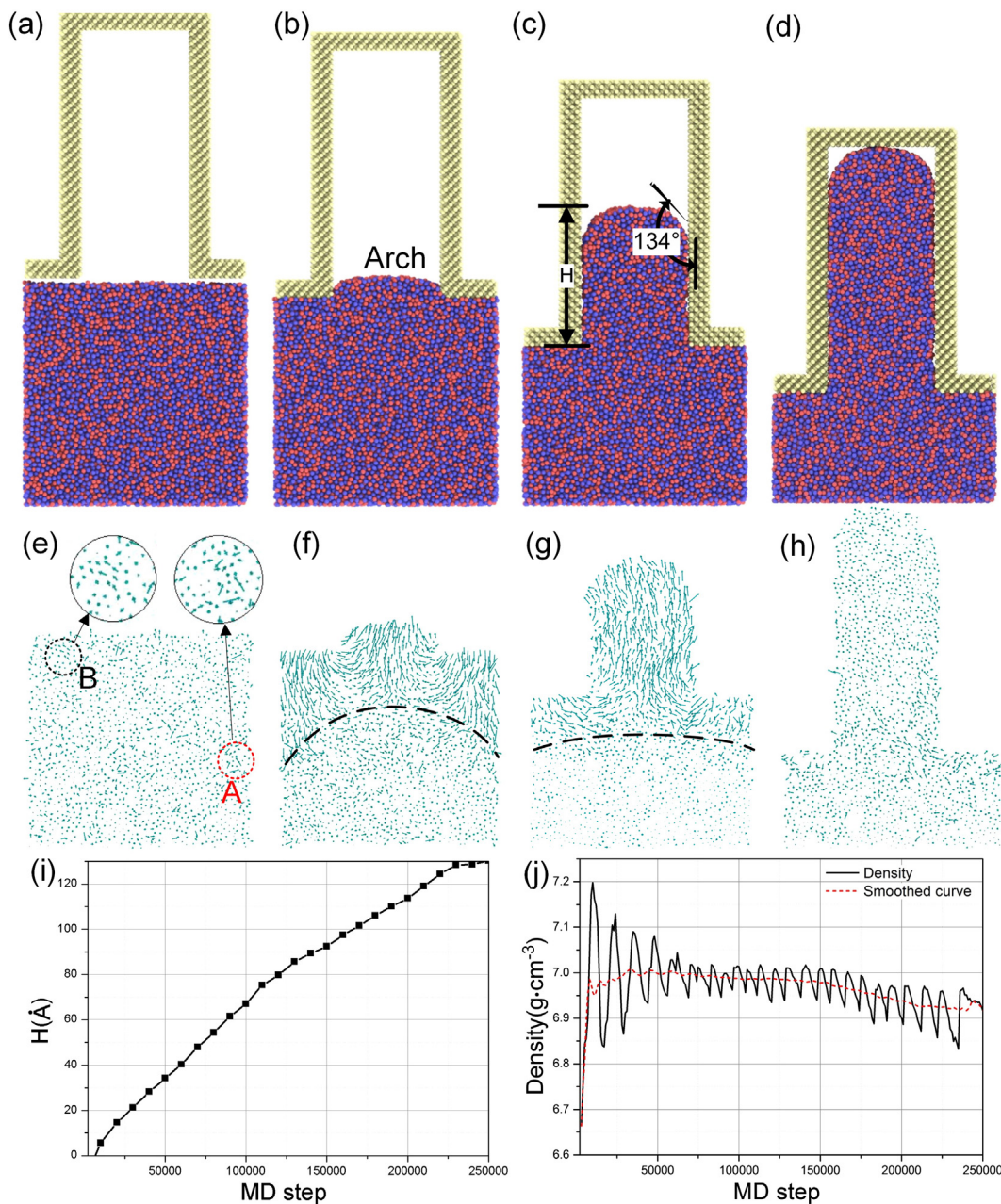
Fig. 3. (a–d) The snapshots of the nanoimprint process cutaway views and (e–h) the displacement vectors of the MG atoms on the profile at 0 ps, 10 ps, 100 ps and 250 ps. (i) H vs. time relationship and (j) density curve of residual MGs.

the stamp. After 10 ps the stamp begins to be pressed onto the MG film and an arch is forming at the entrance of the groove, as shown in Fig. 3b. The MG atoms are then squeezed into the groove and the arch is still on the top of the grating, as displayed in Fig. 3c. The angle marked between the silicon stamp and the MGs is a dynamic contact angle, about 134°. The fully filled grating is shown in Fig. 3d. Fig. 3e–h demonstrates the displacement vectors of the MG atoms on the profiles in the corresponding time. The MGs remain stable under 800 K without any external action. A few atoms marked by A are found jumping out of their initial positions alone and the highly collective hopping process marked by B also occurs, as shown in Fig. 3e, which is a particular mechanism of diffusion behavior in MGs. When the arch begins to appear, the surface layer atoms of the film move into the groove but the lower atoms remain quiescent, forming a conspicuous boundary between the moving atoms and the still atoms, as pointed out by the dash line in Fig. 3f. This is a typical backward extrusion process and only the atoms in the surface layer near the entrance take part in the deformation. The thickness of the moving layer drops to about 30 Å when the mold filling process becomes steady, as shown in Fig. 3g.

The H vs. time relationship is shown in Fig. 3i. The grating is growing up constantly until the groove is filled up at about 230 ps. It is a convex curve, demonstrating that the filling speed has a downward trend throughout the process. As shown in Fig. 3j, the density data of the residual MGs are presented to assess the volume changes. The fluctuation is very obvious in the density curve, which is caused by the extremely high imprint speed owing to the high pressure. The dotted curve is the smoothed density curve, which increases rapidly from 6.65 g·cm^{-3} to around 7.00 g·cm^{-3} in 40 ps and then maintains at a high level, proving that the volume compression occurs in the film.

Fig. 4b shows the relationship of H vs. time with different TF values under 48 nN force. The curves are classified into three groups for further analysis: $TF < 60$ Å ($1Wg$), 60 Å ($1Wg$) $< TF < 120$ Å ($2Wg$) and $TF > 120$ Å ($2Wg$). When TF is less than or close to $1Wg$ (45 Å or 60 Å), the groove is not filled up. The thicker film (60 Å) leads to a higher grating and a faster

mold filling speed; when TF is between $1Wg$ and $2Wg$ (80 Å, 100 Å or 120 Å), the groove can be filled up. The thicker the film is, the slower the grating grows; when TF is more than $2Wg$ (180 Å, 240 Å or 300 Å), the situation becomes more complex. The thicker film curves conduct a lower mold filling speed at the beginning, but exceed the thinner film curves at the height of about 90 Å ($1.5Wg$) finally. Noteworthily, this phenomenon also occurs under the force of 32 nN (Fig. 4a) and 64 nN (Fig. 4c). The pressure does not affect the internal relation summarized in Fig. 4b, and just stretches or compresses the time-axis. The distinction of the curves enlarges as the pressure decreases. In the actual imprint process, high pressure will crush the fragile silicon stamps, thus much smaller force than 32 nN will be applied, leading to obvious thickness effect.

Fig. 4d displays the effect of the thickness more obviously and intuitively, where X-axis is the TF, Y-axis is the H, and the color represents the MD step relating to time. The dark region means incomplete filling and the data of the TF less than 45 Å are absent. We can easily find a peak area with the TF a bit larger than $1Wg$ (60 Å), implying less filling time and faster filling speed. No other area can reach a certain H faster than the peak area. In $H > 1.5Wg$ (90 Å) region, the area with large TF also behaves well but not economically. As the MG crystallization after long-time relaxation will result in the rapidly dropping of properties, the imprinting time is an important parameter which should be controlled strictly. Thus, we can arrive at a conclusion that 60 Å is the optimal TF when imprinting a 60 Å width grating, i.e., the TF close to the groove width of the imprinting stamp will lead to a complete, efficient and economical filling process. It should be pointed out that the duty cycle of the grating pattern on the stamp is 50% and if not, the optimal thickness may be slightly different.

3.2. The resistance of boundary condition and capillary force

Plane Poiseuille flow is a classical model for the laminar flow of a viscous fluid in space between parallel plates, which can be used in the investigation of the mold filling process. Considering the rise of
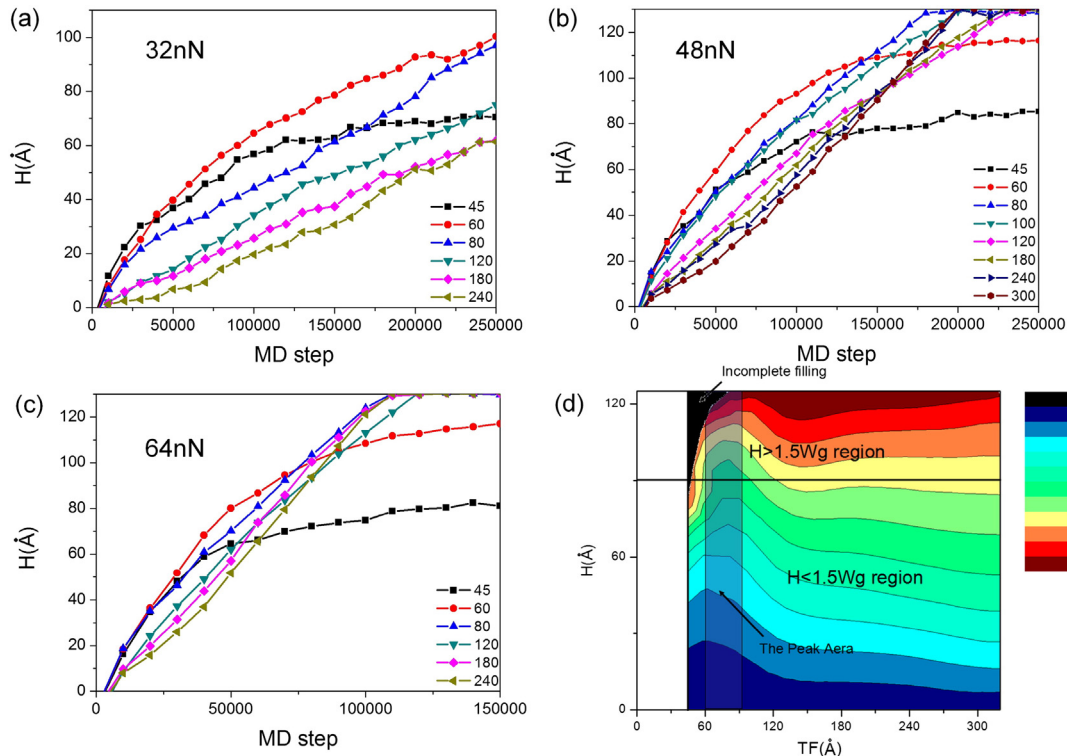
Fig. 4. The relationship of H vs. time: (a) under 32 nN force, (b) under 48 nN force and (c) under 64 nN force. (d) The time nephogram for nanoimprint.

capillary contributions in nanoscale, we modify the model of plane Poiseuille flow by combining the capillary contributions [5]:

$$P = \frac{12\eta}{t}\left(\frac{l}{b}\right)^2 - \frac{2(b+c)\gamma\cos\theta}{bc} \qquad (1)$$

where η is the viscosity, γ is the MG-vacuum surface tension, θ is the dynamic contact angle, b and c are the width and length of the mold respectively, l is the height of the grating, t is the filling time and P is the required pressure. The first term arises from plane Poiseuille flow and the width of flow channel has enormous influence on the filling speed. The second term is the capillary contribution, which will play a crucial role in nanosize due to the size effect. The capillary pressure is positive benefiting for filling when $\theta < 90°$, and is negative obstructing filling when $\theta > 90°$. Since the angle (about 134°) is larger than 90° measured in Fig. 3c, the capillary force obstructs the specimen flow.

Fig. 5 shows the pressure nephograms of three typical thicknesses (60 Å, 120 Å and 240 Å) under the force of 48 nN, in which the pressure is obtained from the per-atom stresses. The model is divided into 2 Å × 2 Å cells. The per-atom stresses in every cell are summed, and divided by $-d \times V$, where d is the dimension and V is the volume of the cell, so as to obtain the pressure of each cell and draw out the pressure nephograms. The blue parts on the top of the MG grating are the surface tension.

As shown in Fig. 5g, the mold filling process can be regarded as a combination of a plane Poiseuille flow marked with A and a similar flow marked with B. The displacement vectors of the MGs shown in Fig. 3f and Fig. 3g demonstrate that the region marked with B is a half open flow or a plane Poiseuille flow with an infinite width (b), where the atomic migration is only affected by the silicon stamp boundary in the upside as the atoms contacting with stamp will adhere to the silicon stamp. The boundary condition changes when the residual film becomes thin enough and the effect of lower boundary takes action. It
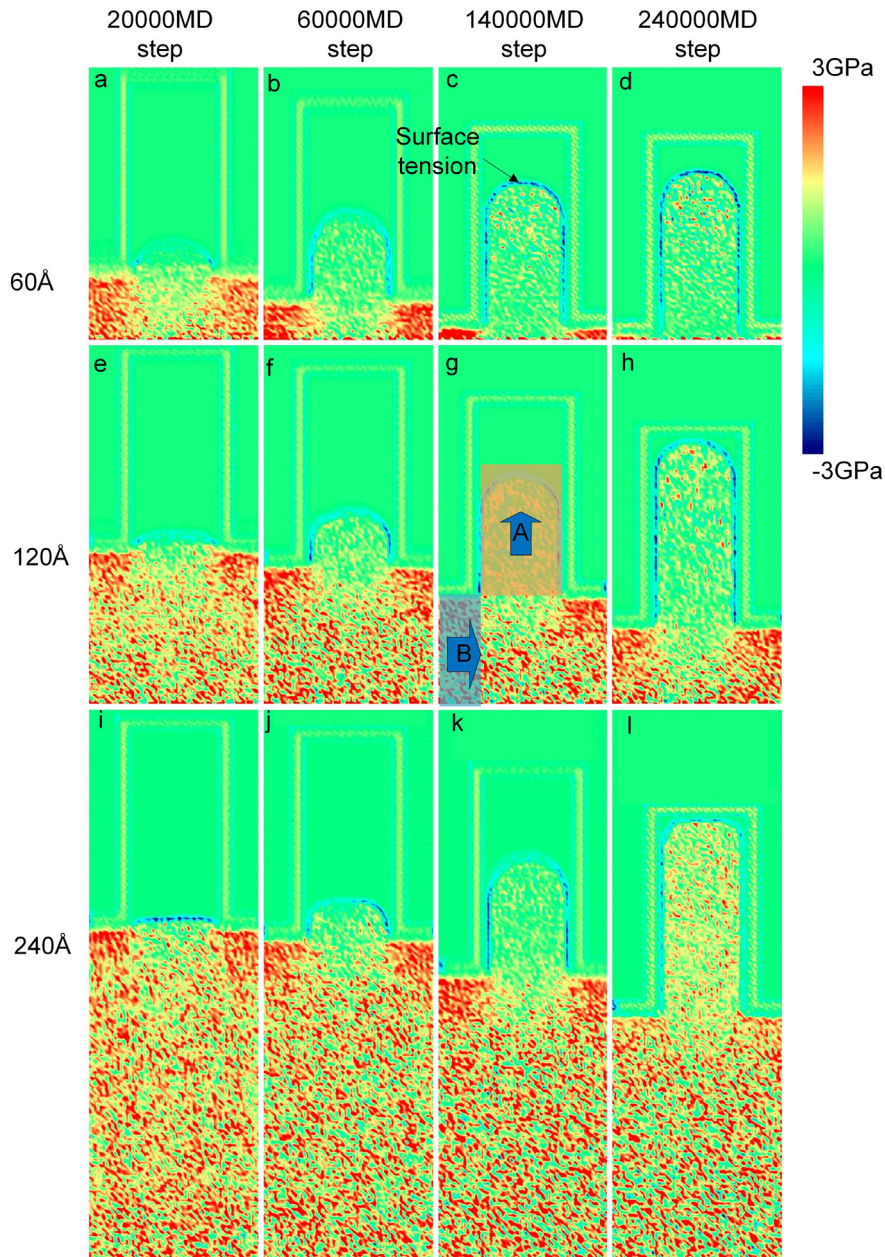
Fig. 5. The pressure nephograms of nanoimprint under three different thicknesses (60 Å, 120 Å and 240 Å). (For interpretation of the references to color in this figure, the reader is referred to the web version of this article.).
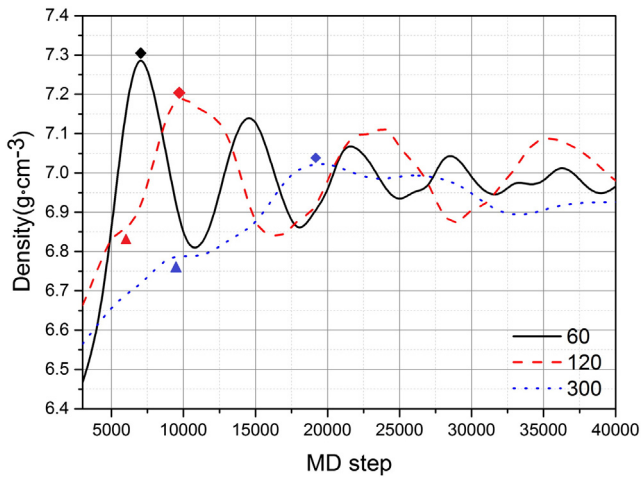
Fig. 6. Density changes under different thicknesses (60, 120, 300 Å) in the first 40 ps. (For interpretation of the references to color in this figure, the reader is referred to the web version of this article.).

turns to another plane Poiseuille flow with a decreasing width (b), just as depicted in Fig. 5a–d. As no solid–vacuum interface exists here, the second term is absent. With a smaller width (smaller b), the atomic moving channel is narrowed and the flow resistance rises, resulting in heavily pressure drop. That is why the growth velocity of the mold filling process with thin film thickness conducts a downward trend as shown in Fig. 3i.

In region A, the width is fixed and the effect of capillary force works. The filling will not begin until the required pressure (P) is positive in Eq. (1). Fig. 6 depicts the relationship of the density of residual MG film vs. time under different thicknesses (60, 120, 300 Å) in the first 40 ps. Step occurs on both blue (120 Å) and red (300 Å) curves marked by triangles and is not obvious on black (60 Å) curve as the slope is too high. The mold filling process is found to be stagnated before reaching these steps. After MGs begin to flow into the groove, the pressure is released, resulting in these steps. It is easy to understand that the inlet pressure surpasses the capillary force and the required pressure (P) becomes positive right at these steps. Additionally, the films with different thicknesses have different responses to the press of stamp. The density of the thicker film (300 Å) needs more time than the thinner one (120 Å) when reaching both the triangles (the steps) and the rhombuses (the first peaks), meaning that the pressure surpasses the capillary force later and the filling speed is slower with the thicker TF. This trend is also demonstrated in Fig. 4. With the same compressibility, the thicker film has a larger compression space and costs much more

time to fill the space, which can be regarded as a system response delay. In actual experiments, the pressure is much smaller and the imprint process is not a strictly closed extrusion, and the delay will be more obvious. Therefore, it is important to consider the effect of film thickness and select an appropriate thickness in nanoimprinting MGs.

3.3. Structural evolutions

The inner structures of MGs during the cooling process and the mold filling process are characterized by a radical Voronoi tessellation [31]. The atomic radii of copper and zirconium are set as 1.28 Å and 1.60 Å, respectively. The particle positions are taken as the Voronoi cell centers. The shape of each Voronoi cells can be defined using the Voronoi index, $<n_3, n_4, n_5, n_6>$, where n_x is the number of faces with x edges. Fig. 7a shows the fractions of six predominant clusters in the alloy during the cooling process, including perfect ICO cluster <0 0 12 0> and ICO-like clusters <0 1 10 2>, <0 2 8 1>, <0 2 8 2>, <0 3 6 3>, and <0 3 6 4>, which agrees with the results reported in reference [32]. The fractions of ICO or ICO-like clusters increase rapidly when the temperature decreases to the glass transition temperature. The perfect ICO cluster has the largest increase (about 368%), followed by <0 2 8 1> (132%) and <0 2 8 2> (147%). When the temperature is 300 K, <0 2 8 2> is the most popular cluster, about 6.4%. As shown in Fig. 7b, the fractions of ICO or ICO-like clusters decrease after being heated to 800 K. Among these clusters, <0 2 8 2> is still the most popular cluster, about 4.1% in the billets. But the fraction comes up to 5.1% in the residual films during the mold filling process. The MGs tend to own more ICO or ICO-like clusters under pressure. We also find that the fractions of ICO or ICO-like clusters sharply decrease after the filling process in the new-born grating. The clusters in the grating are much lesser than that in the residual film whether the grating is growing or completely formed. The fraction of full ICO in the grating is only 28% of that in the residual film. The grating is free of pressure when it is growing as shown in Fig. 6k and the pressure comes back when the filling process is completed as shown in Fig. 6l. But the distinction of the fractions of ICO between these two situations does not occur, indicating that the structural evolutions are pressure-independent and the breaks of the original mapping of ICO are mainly caused by the flow of MGs.

It was reported that the ICO clusters in the MGs were not independent [20]. Instead, they overlapped together and formed a network, which was considered to be the medium-range order in MGs. To characterize the order, the positions of full ICO atoms are extracted. If the two central atoms are the nearest neighbors, the clusters are defined as neighbors. Fig. 8a shows the aggregated cluster distribution in the grating and the original MG billets. The fraction of the single cluster is about 47% in the grating, larger than that in the billets (about 41%).
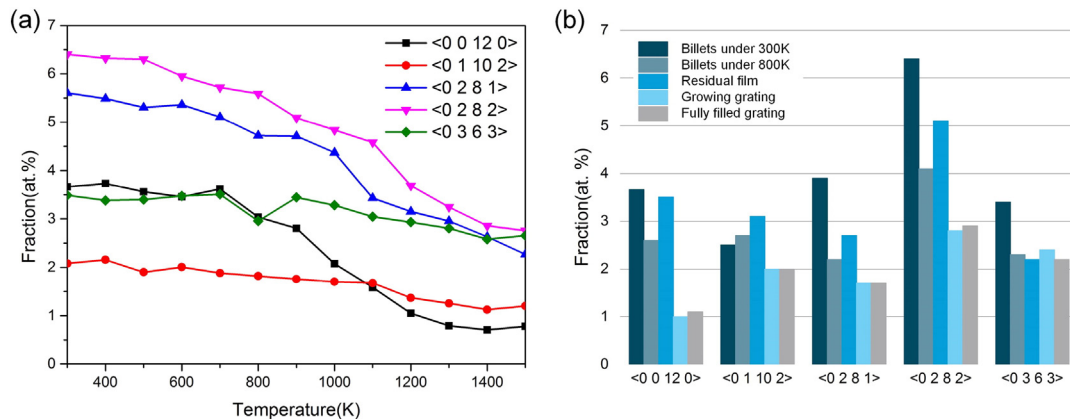
Fig. 7. The fractions of ICO or ICO-like clusters during (a) the cooling process and (b) the mold filling process.
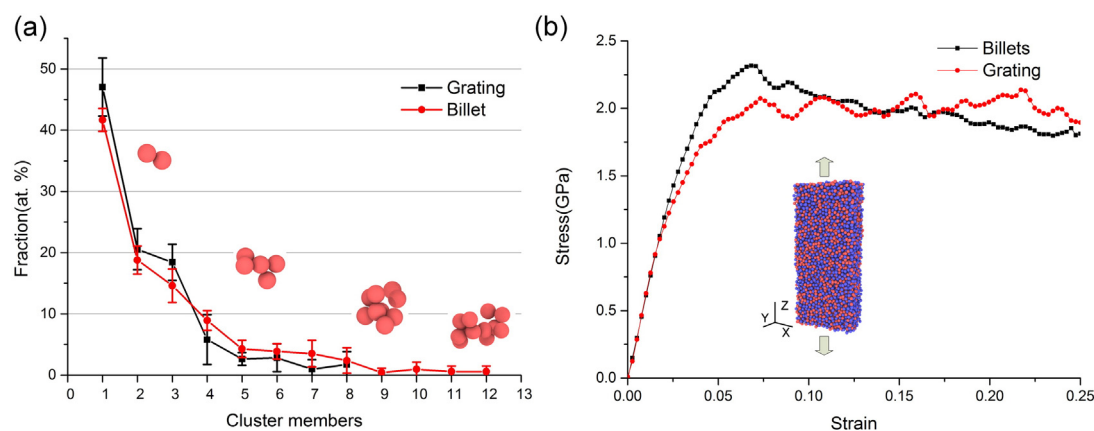
Fig. 8. (a) The distribution of the size of aggregated cluster and (b) stress–strain curves of the grating and billets.

The fractions of two and three members aggregated clusters are also larger in the grating. But the large size (larger than four) aggregated clusters are more common in the billets. There even exist super aggregated clusters containing twelve members. The largest aggregated cluster in the grating only has eight members. Based on current studies, the fraction of full ICO has been hypothesized to be an indicator of the plastic behavior of MGs, which is resistant to the atomic migration [18] and the dynamic arrest effect is much more significant in aggregated clusters than in single ICO [33]. The larger aggregated cluster owns much denser bonds in local area, where the restricted atoms need more activation energy to jump out. Here the processed MGs have lesser full ICO and smaller aggregated clusters, indicating a better plastic performance.

Subsequently, we cool down the grating to 300 K rapidly, relax it for 20 ps, and carry out uniaxial tensile tests. The size of the specimens is $50 \times 25 \times 120$ Å^3 and the periodic boundary condition is applied on Y and Z dimensions, as indicated in Fig. 8b. The strain is exerted on the Z-axis and the strain rate is set as 1e8/s. The stress–strain curve of the billets reaches the ultimate tensile stress (about 2.4 GPa) at the strain of 0.068, but falls steady until the end. For the grating, the case is different. The ultimate tensile stress is only about 2 GPa and the curve hardly changes in later stages, showing a better plasticity. Though the MD models have their spatiotemporal limitations, the MD results reveal insightful trends that the processed MGs own a better plastic performance. The nanoimprint process is also an isothermal annealing process, which will result in crystallization and dropping of properties of MGs gradually. Therefore, the improvement of the plastic performance can hardly be observed in the experiments. If we can add a mechanical extrusion in the process of preparing MGs and reduce the annealing time, the plastic performance of MGs may be improved, which needs further experimental verification.

4. Conclusions

In this paper, we construct a MD simulation model for nanoimprinting MG grating. The thermoplastic deformation and structural evolutions of MGs are investigated in detail. We find that the mold filling speed is obviously affected by the initial film thickness. According to a modified equation of plane Poiseuille flow, the boundary condition and capillary force are proved to play critical roles, which reasonably explain the effect of initial film thickness. Our work provides a useful instruction to obtain MG structures via nanoimprint. The film with the thickness approaching the width of the groove is beneficial to perform a complete, efficient and economical filling process. We also show the structural evolutions of the short-range and middle-range orders in the MGs during the cooling process and mold filling process. The results suggest that the processed MGs have a better plastic performance than billets, which may be a viable method to improve the plasticity of MGs.

References

[1] J.H. Jeong, Y.S. Choi, Y.J. Shin, J.J. Lee, K.T. Park, E.S. Lee, S.R. Lee, Flow behavior at the embossing stage of nanoimprint lithography, Fibers Polym. 3 (2002) 113–119.
[2] Y. Hirai, T. Konishi, T. Yoshikawa, S. Yoshida, Simulation and experimental study of polymer deformation in nanoimprint lithography, J. Vac. Sci. Technol. B 22 (2004) 3288–3293.
[3] H.D. Rowland, A.C. Sun, P.R. Schunk, W.P. King, Impact of polymer film thickness and cavity size on polymer flow during embossing: toward process design rules for nanoimprint lithography, J. Micromech. Microeng. 15 (2005) 2414.
[4] F. Hua, Y. Sun, A. Gaur, M.A. Meitl, L. Bilhaut, L. Rotkina, J. Wang, P. Geil, M. Shim, J.A. Rogers, Polymer imprint lithography with molecular-scale resolution, Nano letters 4 (2004) 2467–2471.
[5] G. Kumar, H.X. Tang, J. Schroers, Nanomoulding with amorphous metals, Nature 457 (2009) 868–872.
[6] J.P. Chu, J. Jang, J. Huang, H. Chou, Y. Yang, J. Ye, Y. Wang, J. Lee, F. Liu, P. Liaw, Thin film metallic glasses: unique properties and potential applications, Thin Solid Films 520 (2012) 5097–5122.
[7] W.I. Lee, Polymer-flow Analysis During Thermal Nanoimprinting Lithography, Plastics Research Online, 2010.
[8] Y. Hirai, M. Fujiwara, T. Okuno, Y. Tanaka, M. Endo, S. Irie, K. Nakagawa, M. Sasago, Study of the resist deformation in nanoimprint lithography, J. Vac. Sci. Technol. B Microelectron. Nanometer Struct. 19 (2001) 2811.
[9] Y.S. Woo, D.E. Lee, W.I. Lee, Molecular dynamic studies on deformation of polymer resist during thermal nano imprint lithographic process, Tribol. Lett. 36 (2009) 209–222.
[10] J.H. Kang, K.-S. Kim, K.W. Kim, Molecular dynamics study on the effects of stamp shape, adhesive energy, and temperature on the nanoimprint lithography process, Appl. Surf. Sci. 257 (2010) 1562–1572.
[11] P. Sharma, N. Kaushik, H. Kimura, Y. Saotome, A. Inoue, Nano-fabrication with metallic glass—an exotic material for nano-electromechanical systems, Nanotechnology 18 (2007) 035302.
[12] K. Takenaka, N. Saidoh, N. Nishiyama, A. Inoue, Fabrication and nano-imprintabilities of Zr-, Pd-and Cu-based glassy alloy thin films, Nanotechnology 22 (2011) 105302.
[13] K. Takenaka, N. Saidoh, N. Nishiyama, M. Ishimaru, M. Futamoto, A. Inoue, Read/ write characteristics of a new type of bit-patterned-media using nano-patterned glassy alloy, J. Magn. Magn. Mater. 324 (2012) 1444–1448.
[14] J. Chu, H. Wijaya, C. Wu, T. Tsai, C. Wei, T. Nieh, J. Wadsworth, Nanoimprint of gratings on a bulk metallic glass, Appl. Phys. Lett. 90 (2007) 034101.
[15] G. Kumar, J. Blawzdziewicz, J. Schroers, Controllable nanoimprinting of metallic glasses: effect of pressure and interfacial properties, Nanotechnology 24 (2013) 105301.
[16] Y.H. Liu, G. Wang, R.J. Wang, M.X. Pan, W.H. Wang, Super plastic bulk metallic glasses at room temperature, Science 315 (2007) 1385–1388.
[17] S. Takeuchi, K. Edagawa, Atomistic simulation and modeling of localized shear deformation in metallic glasses, Prog. Mater. Sci. 56 (2011) 785–816.
[18] Y. Cheng, A.J. Cao, H. Sheng, E. Ma, Local order influences initiation of plastic flow in metallic glass: effects of alloy composition and sample cooling history, Acta Mater. 56 (2008) 5263–5275.
[19] S. Hao, C. Wang, M. Kramer, K. Ho, Microscopic origin of slow dynamics at the good glass forming composition range in $Zr_{1-x}Cu_x$ metallic liquids, Journal of Applied Physics 107 (2010) 053511.

[20] H. Sheng, W. Luo, F. Alamgir, J. Bai, E. Ma, Atomic packing and short-to-medium-range order in metallic glasses, Nature 439 (2006) 419–425.

[21] C.C. Wang, C. Wong, Different icosahedra in metallic glasses: stability and response to shear transformation, Scr. Mater. 66 (2012) 610–613.

[22] M. Mendelev, D. Sordelet, M. Kramer, Using atomistic computer simulations to analyze x-ray diffraction data from metallic glasses, J. Appl. Phys. 102 (2007) 043501.

[23] F. Li, X. Liu, Z. Lu, Atomic structural evolution during glass formation of a Cu–Zr binary metallic glass, Comput. Mater. Sci. 85 (2014) 147–153.

[24] J. Tersoff, Modeling solid-state chemistry: interatomic potentials for multicomponent systems, Phys. Rev. B 39 (1989) 5566.

[25] L. Xie, P. Brault, A.L. Thomann, L. Bedra, Molecular dynamic simulation of binary Zr_xCu_{100-x} metallic glass thin film growth, Appl. Surf. Sci. 274 (2013) 164–170.

[26] T. Egami, Y. Waseda, Atomic size effect on the formability of metallic glasses, J. Non-Cryst. Solids 64 (1984) 113–134.

[27] M. Parrinello, A. Rahman, Strain fluctuations and elastic constants, J. Chem. Phys. 76 (1982) 2662–2666.

[28] Z. Lu, J. Li, H. Shao, H. Gleiter, X. Ni, The correlation between shear elastic modulus and glass transition temperature of bulk metallic glasses, Appl. Phys. Lett. 94 (2009) 91907.

[29] G. Duan, D. Xu, Q. Zhang, G. Zhang, T. Cagin, W.L. Johnson, W.A. Goddard III, Molecular dynamics study of the binary $Cu_{46}Zr_{54}$ metallic glass motivated by experiments: glass formation and atomic-level structure, Phys. Rev. B 71 (2005) 224208.

[30] S. Plimpton, Fast parallel algorithms for short-range molecular dynamics, J. Comput. Phys. 117 (1995) 1–19.

[31] F. Aurenhammer, Voronoi diagrams—a survey of a fundamental geometric data structure, ACM Comput. Surv. (CSUR) 23 (1991) 345–405.

[32] L. Ward, D. Miracle, W. Windl, O.N. Senkov, K. Flores, Structural evolution and kinetics in Cu–Zr metallic liquids from molecular dynamics simulations, Phys. Rev. B 88 (2013) 134205.

[33] S. Hao, C. Wang, M. Li, R. Napolitano, K. Ho, Dynamic arrest and glass formation induced by self-aggregation of icosahedral clusters in $Zr_{1-x}Cu_x$ alloys, Phys. Rev. B 84 (2011) 064203.